Supplementary information for

MgO-Fe miscibility at the core-mantle boundary: Implications for the early geodynamo

Author: Jie Deng

Affiliation:

Department of Geosciences, Princeton University, Princeton, NJ 08544, USA.

Email: jie.deng@princeton.edu

Contents of this file

Texts S1, S2, S3
Figures S1, S2, S3, S4
Tables S1, S2

Text S1 Construction of Machine learning potential

1.1. DeePMD Approach

The DeePMD approach adopts an end-to-end strategy (Wang et al., 2018; Zhang et al., 2018) and does not make *a priori* assumptions about the form of the descriptor but rather uses a deep neural network to determine its form based only on the spatial location, in a suitably defined coordinate frame, of the neighboring atoms. Neural networks are widely used in the development of machine learning potentials because they are, in principle, capable of approximating any continuous function to arbitrary accuracy (Deng and Stixrude, 2021b; Hornik et al., 1989; Lorenz et al., 2004). With DeePMD, one uses a neural network to find the functional form of the descriptor and a second neural network (fitting network) to determine the form of the potential energy surface. The fitting network is composed of three layers with 240 nodes in each layer. A cutoff of 6 Å is employed to describe the atomic local environments. The loss function is defined as

$$L(p_\epsilon, p_f, p_\xi) = p_\epsilon \Delta\epsilon^2 + \frac{p_f}{3N}\sum_i |\Delta \boldsymbol{F}_i| + \frac{p_\xi}{9}\|\Delta\xi\|^2, \quad \text{(S1)}$$

where p_ϵ, p_f, p_ξ are tunable prefactors for difference between the MLP prediction and training data. ϵ is the energy per atom; $\boldsymbol{F}_i$ atomic force of atom i ; ξ the virial tensor divided by N; N the numbrer of atoms. We adopt the conventional setting of increasing both p_ϵ and p_ξ from 0.02 to 1 while decreasing p_f from 1000 to 1 over the course of training.

1.2. *Ab initio* calculations

Ab initio calculations were performed using Vienna Ab Initio Simulation Package (VASP) (Kresse and Furthmüller, 1996). We used the projector augmented wave (PAW) method (Kresse and Joubert, 1999) as implemented in VASP (Kresse and Furthmüller, 1996) and PBEsol approximation (Perdew et al., 2008). We use the PBEsol approximation as we have previously found that it yields good agreement with experimental measurements of physical properties of silicates and oxides (Deng and Stixrude, 2021a; Holmström and Stixrude, 2015; Scipioni et al., 2017). The core radii are O: 0.820 Å ($2s^2 2p^4$), Mg: 1.058 Å ($2p^6 3s^2$), Fe: 1.164 Å ($3p^6 4d^7 4s^1$). To construct the initial dataset, we perform *ab initio* molecular dynamics (AIMD) simulations with relatively low precision settings: energy cutoff of 500 eV, energy cutoff of 10^{-4} eV, and Gamma-point only k-mesh. AIMD simulations are performed in the NVT ensemble (constant number of atoms, volume, and temperature) using the Nosé-Hoover thermostat (Hoover, 1985) and run for 5-20 ps with 1 fs time step. We assume thermal equilibrium between ions and electrons via the Mermin functional (Mermin, 1965).

The major focus of this study is the exsolution process at the core-mantle boundary condition. Magnetic fluctuations no longer play a significant role for the liquid iron at this condition (Korell et al., 2019). In addition, (Mg,Fe)O, regardless of liquid or solid phase, will be of low-spin state and have zero net magnetic moment at the pressure and temperature considered (Badro, 2014; Karki et al., 2018). The influence of spin polarization on the MgO-Fe phase relation is likely to be small. Therefore, all the calculations are non-spin-polarized following previous studies (Wahl and Militzer, 2015; Wilson et al., 2023).

The configurations generated by these AIMD simulations as well as the multithermal and/or multibaric MD simulations were then selected to construct the MLP. The energy, force, and stress of these selected configurations were recalculated at much higher precision with: the energy cutoff that sets the size of the basis set increased from 500 eV to 800 eV (Figure S1), the precision to which the self-consistent solution to the Kohn-Sham equations is lowered from 10^{-4} eV to 10^{-6} eV, and sampling of the Brillouin zone

increased from the Gamma-point only to a 2×2×2 Monkhorst-Pack mesh. We found this high precision recalculation to be important for optimizing the robustness of the MLP (Deng and Stixrude, 2021b) .

Convergence tests of *ab initio* calculations

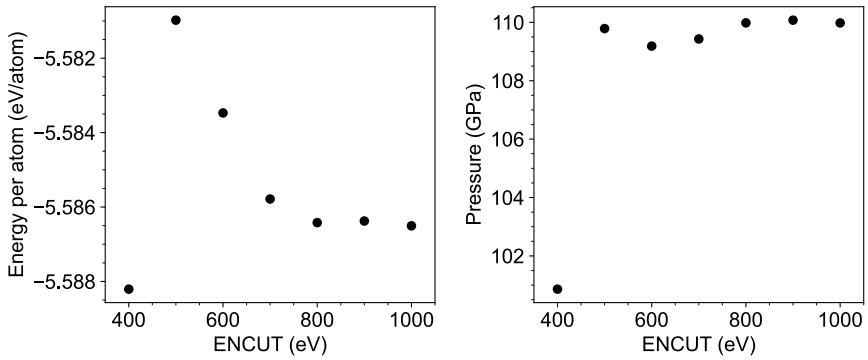

Figure S1. Convergence tests of total energy (a) and pressure (b) with varying energy cutoffs (ENCUT flag in VASP) for a mixture of $Mg_{64}O_{64}Fe_{64}$ at the static condition. An energy cutoff of 800 eV is sufficient to obtain converged results for both energy and pressure.

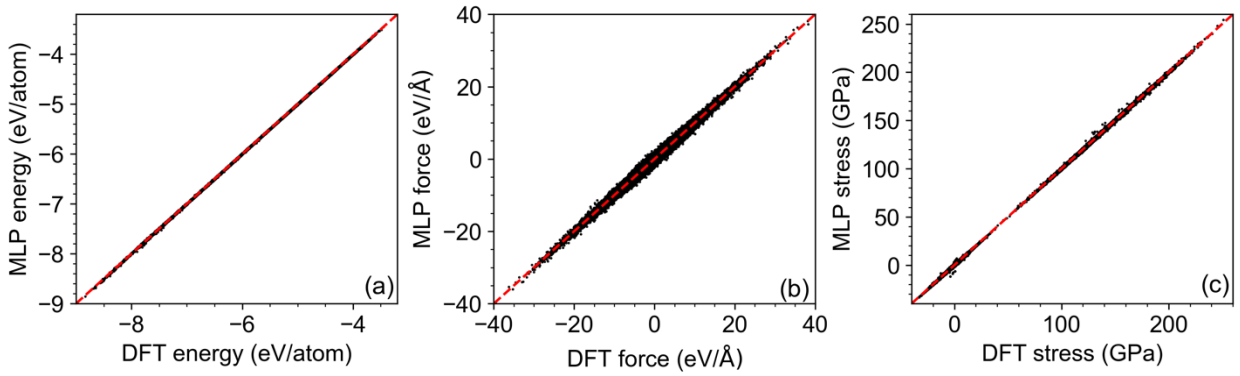

Figure S2. Comparisons of energies (a), atomic forces (b), and stresses (c) between DFT and the machine learning potential (MLP) for all the test data at temperatures up to 8000 K and pressures up to ~200 GPa. 15078 energies, 5988786 force components, and 135702 stress components are included in these comparisons. The red dashed lines are guides for perfect matches.

DFT vs. MLP

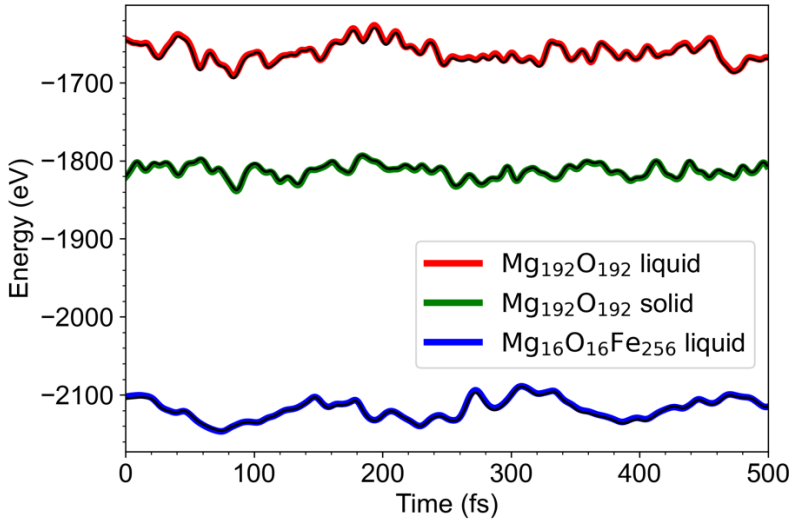

Figure S3. Comparisons of the total energy changes along molecular dynamics trajectories between the DFT (thick colored lines) and MLP potential (thin black lines) for liquid $Mg_{192}O_{192}$ (red), solid $Mg_{192}O_{192}$ (green), and liquid $Mg_{16}O_{16}Fe_{256}$ (green) at 140 GPa and 5000 K. The models used in this simulation contain 432 atoms, and none of the structures in the trajectories were included in the training set. The root mean square error of MLP is 4.9, 2.8, 4.6 meV/atom for liquid $Mg_{192}O_{192}$, solid $Mg_{192}O_{192}$, and liquid $Mg_{16}O_{16}Fe_{256}$, respectively.

Convergence with respect to system size

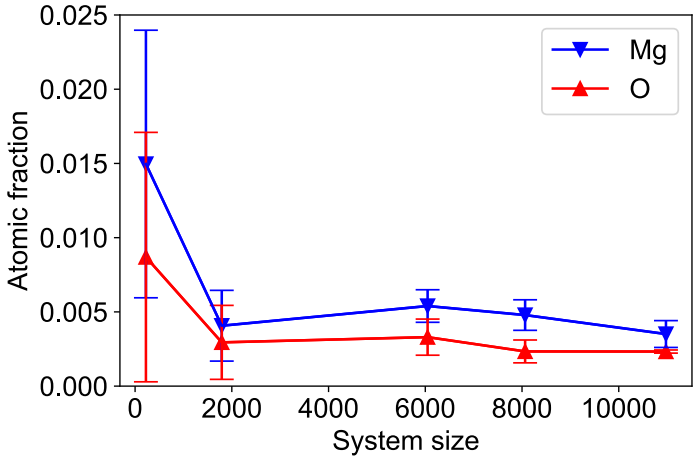

Figure S4. System size convergence test. Equilibrium atomic fractions of Mg (blue circle) and O (red star) atoms in metallic phase as a function of system size (i.e., number of atoms in the system) at 5000 K and 140 GPa. The ratio of the numbers of Mg, O, and Fe are 2:2:3 for all the systems.

Text S2: Thermodynamic model for element partitioning

The exchange coefficients for Mg ($K_D^{\mathrm{Mg}} = \frac{X_{\mathrm{Mg}}^{\mathrm{met}} X_{\mathrm{O}}^{\mathrm{met}}}{X_{\mathrm{Mg}}^{\mathrm{ox}}}$) and O ($K_D^{\mathrm{O}} = \frac{X_{\mathrm{Fe}}^{\mathrm{met}} X_{\mathrm{O}}^{\mathrm{met}}}{X_{\mathrm{FeO}}^{\mathrm{ox}}}$) are functions of pressure, temperature, and activity. Previous studies suggest that strongest non-ideality arise from interaction between light elements and Fe liquid, compared with silicate and oxide phase (Fischer et al., 2015; Liu et al., 2019). By considering the activity coefficients of light elements in the Fe liquid, one reaches,

$$\log_{10} K_D^{\mathrm{Mg}} = \log_{10} K_{\mathrm{Mg}} - \log_{10} \gamma_{\mathrm{Mg}} - \log_{10} \gamma_{\mathrm{O}}$$

$$\log_{10} K_D^{\mathrm{O}} = \log_{10} K_{\mathrm{O}} - \log_{10} \gamma_{\mathrm{O}}$$

, where K_{i} is equilibrium constant, and γ_{i} is the activity coefficient (i is Mg or O). K_{i} is only a function of pressure P and temperature T for a given system and can be written as

$$\log_{10}(K_{\mathrm{i}}) = a_{\mathrm{i}} + \frac{b_{\mathrm{i}}}{T} + \frac{c_{\mathrm{i}} P}{T}$$

, where parameters a, b and c are related to the changes of entropy, enthalpy and molar volume of the dissociation reaction at reference state.

We use the formalism of (Ma, 2001) to describe γ_{i}

$$\begin{aligned} \log_{10}(\gamma_i) = & -\frac{1}{2.303}\varepsilon_i^i \ln(1 - X_i) \\ & -\frac{1}{2.303}\sum_{i \neq j} \varepsilon_i^j X_j \left(1 + \frac{\ln(1 - X_j)}{X_j} - \frac{1}{1 - X_i}\right) \\ & +\frac{1}{2.303}\sum_{i \neq j} \varepsilon_i^j X_j^2 X_i \left(\frac{1}{1 - X_i} + \frac{1}{1 - X_j} + \frac{X_i}{2(1 - X_i)^2} - 1\right) \end{aligned}$$

, where i and j are MgO, or O. X_{i} is the molar fraction of element i in the metallic phase. ε is the interaction parameter with $\varepsilon_i^j = \varepsilon_j^i$. ε can be further expressed as $\varepsilon_i^j(T) = \frac{1873}{T}\varepsilon_i^j(T = 1873\ K)$.

Text S3 Regression

We fit the exsolution simulation results and previous experiments on ferropericlase-Fe partitioning simultaneously to resolve the thermodynamic parameters. We exclude the data with reported carbon contamination (Du et al., 2019b). Early experiments do not report Mg contents in the liquid Fe and are therefore only used to constrain O partitioning. We first explore fitting the oxygen partitioning independently using data from this study and experimental results from (Asahara et al., 2007; Frost et al., 2010; Ozawa et al., 2008). The goodness of fit (measured by R^2) dramatically drops from 0.93 to 0.74 as long as the four data points reported by (Frost et al., 2010) are included. This is largely due to the conflicting results between (Frost et al., 2010) and (Ozawa et al., 2008) at around 30-70 GPa. We therefore reject the data of (Frost et al., 2010) for fitting.

We then fit both K_D^{Mg} and K_D^{O} simultaneously using the data of this study and (Asahara et al., 2007; Ozawa et al., 2008). Based on F-test, the model with or without a_{Mg} and $\varepsilon_{\mathrm{Mg}}^{\mathrm{Mg}}$ fit the data equally well. As such, a_{Mg} and $\varepsilon_{\mathrm{Mg}}^{\mathrm{Mg}}$ are set to be 0. The negligible roles of a_{Mg} and $\varepsilon_{\mathrm{Mg}}^{\mathrm{Mg}}$ on partitioning are consistent with previous studies on metal-silicate systems (Badro et al., 2018; Du et al., 2019a; Liu et al., 2019). The resulting fitted parameters are listed in Table S3.

Table S1 Summary of exsolution simulations at 140 GPa. N_{Mg}, N_{Fe}, and N_O are the numbers of Mg, Fe, O atoms, respectively. The difference between the composition of the bulk system and the sum of those of ferropericlase and metallic liquid yields the composition of the corresponding interface.

T(K)	Bulk system			Ferropericlase			Metallic liquid			$\log_{10}K_D^{Mg}$	$\log_{10}K_D^{O}$
	N_{Mg}	N_{Fe}	N_O	N_{Mg}	N_{Fe}	N_O	N_{Mg}	N_{Fe}	N_O		
5000	3136	4707	3136	1980.2	5.0	1986.6	8.4	2370.6	5.6	–5.09	–0.04
5000	738	4704	738	506.5	2.5	508.3	25.2	4313.3	23.7	–4.50	0.03
5500	738	4704	738	272.6	2.4	274.1	14.7	3819.0	68.1	–4.18	0.29
5500	1476	8364	2520	865.9	14.6	879.5	24.2	6819.2	616.5	–3.56	0.66
5000	1476	8364	2520	767.7	24.6	789.1	8.1	6444.8	502.0	–4.06	0.33
4500	1476	8364	2520	651.7	34.4	655.5	2.0	6108.0	360.8	–4.73	0.02
5000	1476	7525	3358	780.3	19.9	798.3	16.5	5561.3	1048.4	–3.39	0.73
4500	1476	7525	3358	577.0	30.9	602.4	8.5	4954.2	807.3	–3.66	0.37
4000	1476	7525	3358	511.0	57.4	570.4	1.1	4583.0	574.3	–4.57	–0.01
5500	2088	3456	2520	1755.8	47.2	1802.4	7.8	2511.7	161.8	–3.74	0.33
5000	2088	3456	2520	1202.8	29.9	1241.9	1.4	1612.9	33.2	–4.75	–0.09
5000	2088	3110	2866	1313.5	58.7	1364.2	1.8	1338.5	130.1	–3.94	0.28
5000	2088	3110	2866	1434.9	48.2	1478.3	2.7	1605.3	190.5	–3.79	0.46
5500	2304	3456	2304	1767.6	5.1	1771.9	23.7	2426.5	14.0	–4.26	0.29

Table S2 Summary of previous experimental results on ferropericlase-Fe element partitioning. Experiments with reported carbon and sulfur contamination are excluded. (see the content in a separate supplementary file)

Table S3. Fitted parameters of exchange coefficients. The pressure dependence of Mg is not resolved.

	a	b (K)	c (K/GPa)	ε_{Mg}^{i}	ε_{O}^{i}
Mg	0	–24133±215	n.a.	0	–48.72±2.96
O	1.82±0.09	–6704±252	–11.53±1.63	–48.72±2.96	–9.17±0.87

n.a. Not applicable.

Reference

Asahara, Y., Frost, D.J., Rubie, D.C., 2007. Partitioning of FeO between magnesiowustite and liquid iron at high pressures and temperatures: Implications for the composition of the Earth's outer core. Earth and Planetary Science Letters 257, 435-449.

Badro, J., 2014. Spin Transitions in Mantle Minerals. Annual Review of Earth and Planetary Sciences, Vol 42 42, 231-248.

Badro, J., Aubert, J., Hirose, K., Nomura, R., Blanchard, I., Borensztajn, S., Siebert, J., 2018. Magnesium Partitioning Between Earth's Mantle and Core and its Potential to Drive an Early Exsolution Geodynamo. Geophysical Research Letters 45, 13,240-213,248.

Deng, J., Stixrude, L., 2021a. Deep fractionation of Hf in a solidifying magma ocean and its implications for tungsten isotopic heterogeneities in the mantle. Earth and Planetary Science Letters 562, 116873.

Deng, J., Stixrude, L., 2021b. Thermal conductivity of silicate liquid determined by machine learning potentials. Geophysical Research Letters 562, 116873.

Du, Z., Boujibar, A., Driscoll, P., Fei, Y., 2019a. Experimental Constraints on an MgO Exsolution-Driven Geodynamo. Geophysical Research Letters 46, 7379-7385.

Du, Z., Deng, J., Miyazaki, Y., Mao, H.-k., Karki, B.B., Lee, K.K.M., 2019b. Fate of Hydrous Fe-Rich Silicate Melt in Earth's Deep Mantle. Geophysical Research Letters 46, 9466-9473.

Fischer, R.A., Nakajima, Y., Campbell, A.J., Frost, D.J., Harries, D., Langenhorst, F., Miyajima, N., Pollok, K., Rubie, D.C., 2015. High pressure metal–silicate partitioning of Ni, Co, V, Cr, Si, and O. Geochimica et Cosmochimica Acta 167, 177-194.

Frost, D.J., Asahara, Y., Rubie, D.C., Miyajima, N., Dubrovinsky, L.S., Holzapfel, C., Ohtani, E., Miyahara, M., Sakai, T., 2010. Partitioning of oxygen between the Earth's mantle and core. Journal of Geophysical Research: Solid Earth 115, B02202.

Holmström, E., Stixrude, L., 2015. Spin Crossover in Ferropericlase from First-Principles Molecular Dynamics. Phys Rev Lett 114, 117202.

Hoover, W.G., 1985. Canonical dynamics: Equilibrium phase-space distributions. Phys Rev A 31, 1695-1697.

Hornik, K., Stinchcombe, M., White, H., 1989. Multilayer feedforward networks are universal approximators. Neural Networks 2, 359-366.

Karki, B.B., Ghosh, D.B., Maharjan, C., Karato, S.-i., Park, J., 2018. Density-Pressure Profiles of Fe-Bearing $MgSiO_3$ Liquid: Effects of Valence and Spin States, and Implications for the Chemical Evolution of the Lower Mantle. Geophysical Research Letters 45, 3959-3966.

Korell, J.-A., French, M., Steinle-Neumann, G., Redmer, R., 2019. Paramagnetic-to-Diamagnetic Transition in Dense Liquid Iron and Its Influence on Electronic Transport Properties. Phys Rev Lett 122, 086601.

Kresse, G., Furthmüller, J., 1996. Efficiency of ab-initio total energy calculations for metals and semiconductors using a plane-wave basis set. Computational Materials Science 6, 15-50.

Kresse, G., Joubert, D., 1999. From ultrasoft pseudopotentials to the projector augmented-wave method. Phys Rev B 59, 1758-1775.

Liu, W., Zhang, Y., Yin, Q.-Z., Zhao, Y., Zhang, Z., 2019. Magnesium partitioning between silicate melt and liquid iron using first-principles molecular dynamics: Implications for the early thermal history of the Earth's core. Earth and Planetary Science Letters, 115934.

Lorenz, S., Groß, A., Scheffler, M., 2004. Representing high-dimensional potential-energy surfaces for reactions at surfaces by neural networks. Chemical Physics Letters 395, 210-215.

Ma, Z.T., 2001. Thermodynamic description for concentrated metallic solutions using interaction parameters. Metall Mater Trans B 32, 87-103.

Mermin, N.D., 1965. Thermal Properties of the Inhomogeneous Electron Gas. Physical Review 137, A1441-A1443.

Ozawa, H., Hirose, K., Mitome, M., Bando, Y., Sata, N., Ohishi, Y., 2008. Chemical equilibrium between ferropericlase and molten iron to 134 GPa and implications for iron content at the bottom of the mantle. Geophysical Research Letters 35.
Perdew, J.P., Ruzsinszky, A., Csonka, G.I., Vydrov, O.A., Scuseria, G.E., Constantin, L.A., Zhou, X., Burke, K., 2008. Restoring the Density-Gradient Expansion for Exchange in Solids and Surfaces. Phys Rev Lett 100, 136406.
Scipioni, R., Stixrude, L., Desjarlais, M.P., 2017. Electrical conductivity of SiO_2 at extreme conditions and planetary dynamos. Proceedings of the National Academy of Sciences 114, 9009-9013.
Wahl, S.M., Militzer, B., 2015. High-temperature miscibility of iron and rock during terrestrial planet formation. Earth and Planetary Science Letters 410, 25-33.
Wang, H., Zhang, L., Han, J., Weinan, E., 2018. DeePMD-kit: A deep learning package for many-body potential energy representation and molecular dynamics. Comput. Phys. Commun. 228, 178-184.
Wilson, A.J., Pozzo, M., Davies, C.J., Walker, A.M., Alfè, D., 2023. Examining the power supplied to Earth's dynamo by magnesium precipitation and radiogenic heat production. Physics of the Earth and Planetary Interiors 343, 107073.
Zhang, L., Han, J., Wang, H., Car, R., E, W., 2018. Deep Potential Molecular Dynamics: A Scalable Model with the Accuracy of Quantum Mechanics. Phys Rev Lett 120, 143001.